Astron. Astrophys. 357, 651–660 (2000)

ASTRONOMY AND ASTROPHYSICS

High-resolution observations at λ = 3 mm of the OH 231.8+4.2 molecular outflow

C. Sánchez Contreras[1,2], **V. Bujarrabal**[1], **R. Neri**[3], **and J. Alcolea**[1]

[1] Observatorio Astronómico Nacional (IGN), Ap. 1143, 28800 Alcalá de Henares, Spain (sanchez, bujarrabal, j.alcolea@oan.es)
[2] Departamento de Astrofísica, Facultad CC. Físicas, Universidad Complutense, 28040 Madrid, Spain
[3] IRAM, 300 rue de la Piscine, 38406 St Martin d'Hères, France (neri@iram.fr)

Received 18 November 1999 / Accepted 28 February 2000

Abstract. We present high spatial resolution observations of HCO^+ (J=1–0), SO (J=2_2–1_1), $H^{13}CN$ (J=1–0), SiO (v = 1, J = 2–1), and the continuum at 3 mm from OH 231.8+4.2, taken with the IRAM interferometer at Plateau de Bure. We also report the first detection of NS in circumstellar envelopes. The overall distribution of the emission of all molecules (except for HCO^+ and the SiO maser) is similar to that of CO. The most intense emission arises from a compact, slowly-expanding component around the central star. The rest of the emission comes from gas distributed in a narrow region along the symmetry axis, that flows outwards following a velocity gradient also similar to that found in CO. Our observations show with high accuracy the distribution of the HCO^+ intensity, that is found to be very clumpy and strongly enhanced in the shock-accelerated lobes. We argue that such a distribution is due to the efficient formation of this molecule by shock-induced reactions. An expanding disk or ring around the central star is detected from the SO emission. The characteristic radius and expansion velocity of this structure are 2 10^{16} cm and 6–7 km s^{-1}, respectively. The SiO maser emission could arise from the innermost parts of such a disk. The 3 mm continuum emission seems to be due to cold dust ($\sim$ 20 K) distributed in the lobes of OH 231.8+4.2 as well as from warmer ($\sim$ 55 K) dust located in a compact region surrounding the central star.

Key words: stars: AGB and post-AGB – stars: individual: OH 231.8+4.2 – stars: mass-loss – stars: circumstellar matter – stars: late-type

1. Introduction

OH 231.8+4.2 is a remarkable bipolar nebula that surrounds an M 9 III Mira star (Reipurth, 1987; Cohen, 1981; Kastner et al., 1998). The optical nebula consists of two extended, inflated lobes, oriented at a position angle (PA)$\sim$ 21°, which are flowing at high velocity from the nebula center. Its optical emission-line spectrum indicates that the gas in the lobes has been excited by shock waves (Cohen et al., 1985; Sánchez Contreras et al., 2000 – paper I).

Send offprint requests to: C. Sánchez Contreras

The neutral envelope of OH 231.8+4.2, that has been studied by means of its CO emission (Alcolea et al., 1996; Sánchez Contreras et al., 1997; Alcolea et al., in preparation – hereafter paper III), is found to be very cold ($T_{\rm kin}$ $\sim$ 10 K) and massive ($\sim 1 M_\odot$). This envelope is expanding at low velocity ($\sim$ 10 km s^{-1}) near the equator, while at higher latitudes is affected by a strong axial expansion: deprojected velocities as high as $\sim$ 375 km s^{-1} (relative to the nebula center) are reached at the end of the southern lobe. In contrast to the atomic material, the molecular gas is highly restricted to the symmetry axis of the nebula, showing a high length/width ratio of $\sim$ 10–15. Emission of a large number of molecular species has been detected in OH 231.8+4.2 (e.g. Morris et al., 1987; Sánchez Contreras et al., 1997). This source is classified as O-rich, due to the presence of H_2O, OH, and SiO maser emission (Genzel & Downes, 1977; Bowers & Morris, 1984; Jewell et al., 1991) and the large variety of oxygen bearing molecules. In general, many carbon containing molecules are found in OH 231.8+4.2, suggesting that an active chemistry takes place in this nebula.

The pronounced axial symmetry, the large velocities reached by the gas, and the presence of shocks, are characteristics of the OH 231.8+4.2 nebula that are also frequently observed in post-AGB objects, i.e. objects that have left the Asymptotic Giant Branch (AGB) and are evolving toward the Planetary Nebula (PN) stage. For that reason, the mentioned properties of OH 231.8+4.2 have been interpreted in the overall PNe shaping scenario, i.e. they are thought to be the result of the impact of a recent, highly collimated wind on the old, slowly expanding envelope that was ejected by the star during its AGB evolution (Reipurth, 1987; Sánchez Contreras et al., 1997; Sánchez Contreras et al., 2000; Cohen et al., 1985). We note, however, that the structure and kinematics as well as the presence of shocks in the nebula, are absolutely unexpected for its late-type central star, a Mira variable. Thus, the contradiction between the apparent latter evolutionary stage of the envelope (post-AGB) and that of the central star (on the AGB) poses a problem to determine the evolutionary status of OH 231.8+4.2.

Throughout this paper the nebula distance, luminosity and inclination (with respect to the plane of the sky) have been assumed to be, respectively, $\sim$ 1500 pc, $\sim 10^4$ $L_\odot$, and$\sim$ 36° (with

the north lobe pointing toward the observer). These values are relatively well known, the methods used to their determination being described in Bowers & Morris (1984), Reipurth (1987), Woodward et al. (1989), Kastner et al. (1992), and Shure et al. (1995).

2. Observations and data reduction

We have carried out observations of several molecular lines – HCO^+ (J=1–0), SO (J=2_2–1_1), $H^{13}CN$ (J=1–0), SiO (v = 1, J=2–1), and NS ($^2\Pi_{1/2}$, J=5/2–3/2, parity-e) – and the 3 mm continuum in OH 231.8+4.2, using the IRAM interferometer (Guilloteau et al., 1992) located at Plateau de Bure (French Alps). The observations, except for NS, were made between September 1996 and January 1997, and in February 1999. NS was detected while carrying out a ^{12}CO mosaic in this source, during the 1996–1997 and 1997–1998 winter periods (details of the observation will be given in paper III).

Five or four antennas were used (depending on availability), combining compact and extended array configurations – D (four antennas), C2, B1, and B2 – to obtain a good coverage of the uv-plane. The projected baselines ranged from 15 m to 285 m. Just the 3 mm receivers, operated in double side band, were used. The units of the cross-correlator were placed on the lines of interest and set to bandwidths of 20, 40 and 80 MHz with channel spacings of 0.078, 0.156 and 0.625 MHz (leading to spectral resolutions of $\sim$ 0.3, $\sim$ 0.5, and $\sim$ 2 km s^{-1}, respectively). The channels of the different correlator units (in the lower and upper side bands) in which there was no line emission, were combined to obtain a continuum map. The total frequency band used for the continuum is 210 MHz.

Data calibration was performed following the standard procedure using the IRAM/GAG software package. The visibilities were flux, amplitude, and bandpass calibrated using continuum point sources (quasars) or sources with known spatial structure (CRL 618). Amplitude calibrators were observed at regular time intervals (approximately every 20 minutes). Bandpass calibrators were observed once at the beginning of every run. Antenna-based correction factors were obtained and interpolated in time to obtain those adequate to our source.

The calibration of the visibility phase (except for NS, see paper III) was done relative to that of the OH 231.8+4.2 SiO maser. This line originates in the close stellar surroundings (at distances of a few 10^{14} cm in AGB stars, see e.g. Diamond et al. 1994), so it can be considered as a point-like source given the large distance to the source (Sect. 1) and the resulting beam size in these observations (see below). We have used just the central 6 km s^{-1} of the maser line (Sect. 3.3) to phase-reference our visibilities. The advantage of self-calibration over the use of external phase calibrators is that no interpolation in time of the phase correction factors is needed. This procedure thus reduces the phase noise and yields maps with higher dynamic range. Baseline-based phase calibration has been performed, obtaining phase corrections for each baseline and for every single moment in which OH 231.8+4.2 was observed. Also, a smooth function fitting the variation with time of the antenna-based phase correction factors has been calculated and applied to our data. The final results using both procedures were found to be in good agreement. On the other hand, phase calibration has been also done using an external (point-like) calibrator to test reliability of the self-calibration procedure. In particular, we have checked that no spurious structures appear in the self-calibrated maps and that the total fluxes obtained in both cases are compatible. The absolute coordinates of the SiO maser determined from the standard (external) phase calibration are R.A. = $07^h42^m16^s.93$, Dec. = $-14^\circ\,42'50''.2$ (J2000). The origin in our maps corresponds to that position. The absolute positional error (excluding possible systematic errors) is estimated to be $\sim 0''.1$.

The visibilities were Fourier transformed (using natural weighting) and then CLEANed using the Clark method. The primary beam correction has not been applied to our data. This fact does not substantially affect the intensities of the maps (that are relatively compact compared to the primary beam, $\sim 60''$) except for HCO^+, for which an underestimation of the flux $\sim 15\%$ is expected in the northern clumps at $\sim 15''$ from the center. The continuum emission was subtracted from the molecular emission maps before the CLEANing was done. Note that the observed lines are not expected to be optically thick (an estimate of the HCO^+ line opacity is given in Sect. 3.1.2). For NS, the velocity maps are not shown due to the high noise level. In this case, the continuum has been subtracted directly from the spectrum. The resulting maps and/or spectra for the different lines and the 3 mm continuum are presented in Sect. 3. The gaussian 'clean' beam adopted for image restoration is indicated for each map in their respective figure captions.

We have complemented our HCO^+ interferometric observations with zero-spacing $H^{13}CO^+$ (J = 1–0) and $H^{12}CO^+$ (J = 3–2) data obtained toward the central position of OH 231.8+4.2. The $H^{13}CO^+$ (J = 1–0) spectrum was obtained with the 30 m IRAM radiotelescope at Pico de Veleta (Granada, Spain) in July 1997. The HCO^+ (J = 3–2) transition was observed with the 10.4 m radiotelescope of the Caltech Submillimeter Observatory at Mauna Kea (Hawaii, USA) in November 1998. The FWHM of the beam was in both cases $\sim 27''$. The two spectra are shown in Fig. 4 (Sect. 3).

3. Results

3.1. HCO^+

3.1.1. Structure and kinematics

In Fig. 1 we present the interferometric maps of HCO^+(1–0) for the different LSR velocity channels where emission has been detected. In Fig. 2, a map of the HCO^+ velocity integrated intensity is shown. The HCO^+ emission arises from two opposite, narrow lobes oriented at PA 21°, the symmetry axis of the optical nebula (Sect. 1). Near the center, these lobes are hollow (Fig. 1), with a characteristic radius of $\sim 2''.5$ ($\sim 5.5\,10^{16}$ cm). In the central part of the nebula, the HCO^+ emission seems to be slightly more extended in the equatorial direction than that of ^{12}CO (see Fig. 1 and the CO velocity maps in paper III) and other molecules (see e.g. SO data in Sect. 3.2). In the direction of the

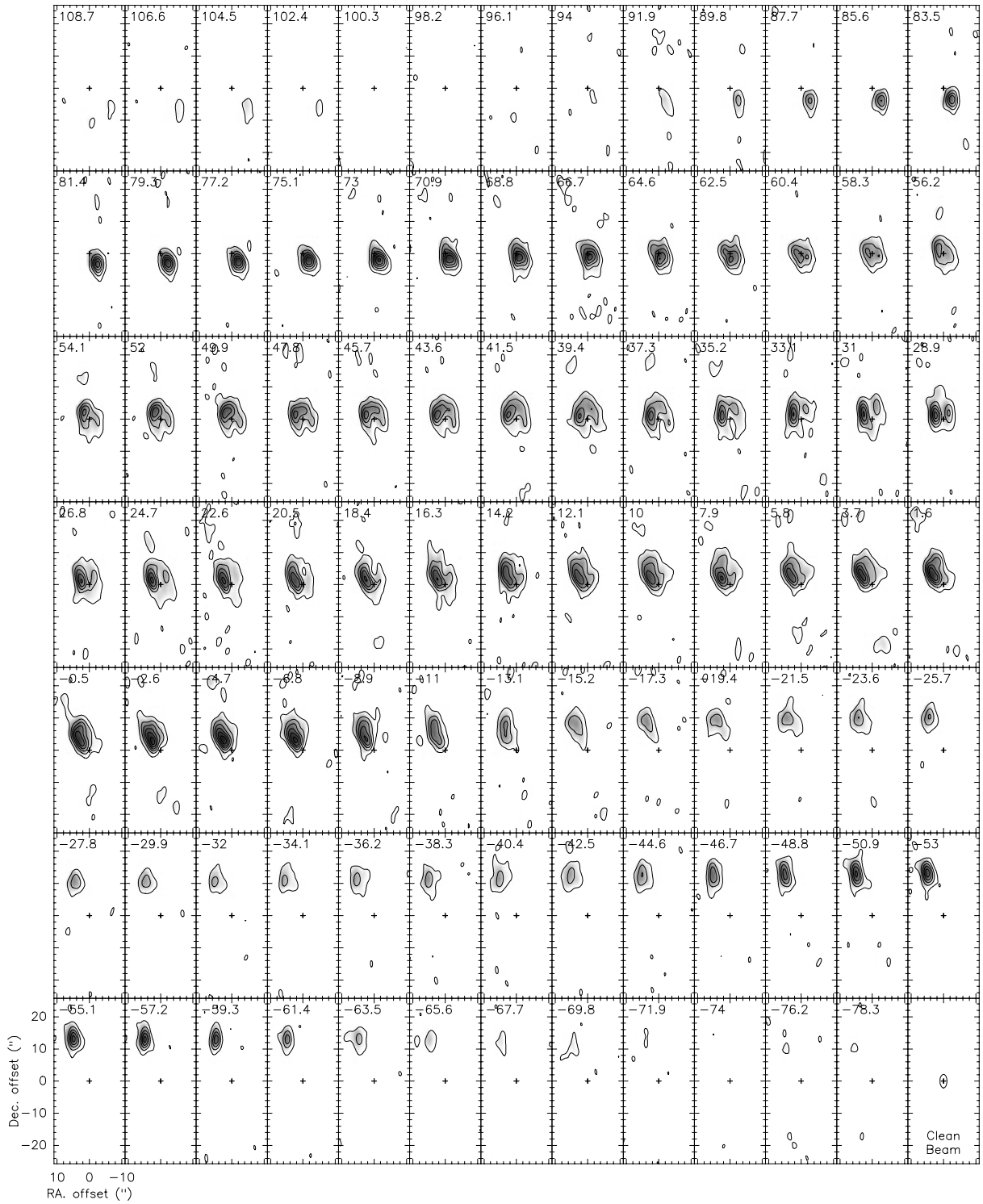

Fig. 1. HCO^+ interferometric maps at different LSR velocities (indicated in the top-right corners; $V_{\rm sys} \sim 33\,{\rm km\,s^{-1}}$). Levels are 10 to 110 by 20 mJy/beam. The rms is ~ 4 mJy/beam. The adopted clean beam has a FWHM of $4\farcs2 \times 2\farcs2$ and is oriented at PA = 0°. Offsets are given with respect to the position of the SiO maser emitting region, (J2000) R.A. = $07^{\rm h}42^{\rm m}16\fs93$, Dec. = $-14°\,42'\,50\farcs2$. The conversion factor from flux units to brightness temperature is 17 K per Jy beam^{-1}.

axis, the HCO^+ emitting region has a total (deprojected) extent of $\sim 7\,10^{17}$ cm and shows a remarkable asymmetry with respect to the equator, the north lobe being almost twice as extended as the southern one. The equatorial asymmetry is also present in the ^{12}CO nebula, but in this case, the south lobe is the largest of the two (with a total, deprojected length of $\sim 1.5\,10^{18}$ cm; see

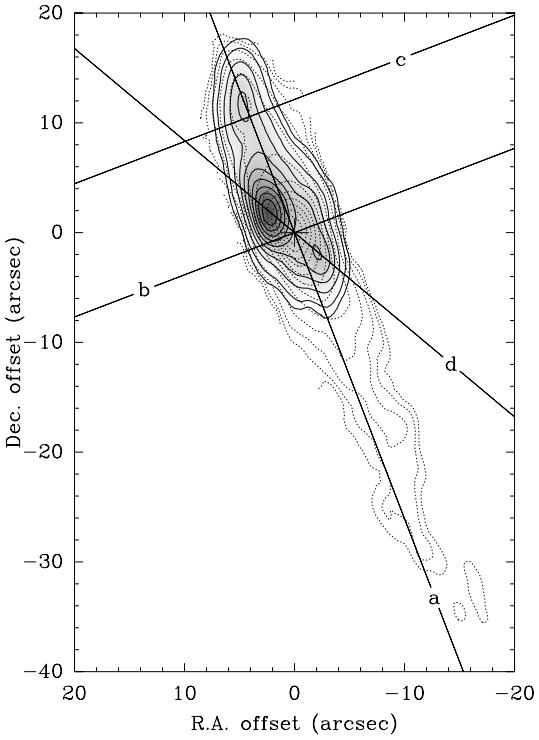

Fig. 2. Map of the HCO^+ velocity integrated intensity (grey scale and solid contours) superimposed on that for ^{12}CO (1–0) (dotted contours; paper III). Levels for the HCO^+ map are 5 and 10 to 100 by 10% of the maximum. For ^{12}CO levels are 1.25, 2.5, 5, and 10 to 100 by 10% of the maximum. We show the directions along which position-velocity diagrams of HCO^+ are presented in Fig. 3.

Fig. 2). However, we note that the extent of the detected HCO^+ emission is limited to the interferometer field of view, that in the case of the present observations is $\sim 60''$, in contrast to $\sim 100''$ for the ^{12}CO mosaic (paper III). Therefore, at the southern tip of the ^{12}CO nebula (at $\sim 30''$ from the center) the HCO^+ emission would be underestimated by a factor 2. On the other hand, the HCO^+ intensity in the north clumps at $\sim 15''$ from the center is underestimated by $\sim 15\%$. The axial asymmetry of the HCO^+ emission is also noticeable. In fact, most of the emission arises from the west side of the nebula.

Our high resolution observations reveal the remarkable clumpiness of the HCO^+ emission. Note, for instance, the intense northern clump flowing at an LSR velocity ~ -50 km s^{-1}, coincident with the outermost northern CO clump, and the southern clumps at ~ 70 and ~ 105 km s^{-1}. Note also that the maximum HCO^+ emission (Fig. 2) arises from a relatively compact clump that is displaced from the nebula center.

The HCO^+ emission shows a clear axial velocity gradient that appears in both the intensity maps per velocity (Fig. 1) and in the position-velocity (p-v) diagram along the nebula axis (direction "a" in Fig. 2) represented in Fig. 3. In particular, the emission from the southern (northern) clumps is red- (blue-) shifted with respect to the systemic velocity ($V_{\rm sys} \sim 33$ km s^{-1}). This velocity gradient is similar to that found for ^{12}CO and other molecules (see below and Sánchez Contreras et al. 1997), indicating that HCO^+ shares the overall axial expansion of the molecular envelope. In Fig. 3, p-v cuts along other selected directions ("b", "c", and "d" in Fig. 2) are given. The p-v diagram along the nebula equator (direction "b") reveals some expansion (at velocity ~ 30 km s^{-1}) in the direction perpendicular to the major axis of the nebula. We note that the figure given above for the expansion velocity can be affected by the mixing within our beam of regions axially expanding. Some expansion (in the direction perpendicular to the nebular axis) is also present at higher latitudes, as the p-v cut along the direction "c" indicates. The expansion velocity derived from this diagram is ~ 15 km s^{-1}. The axial asymmetry of the north lobe can be also appreciated from the previous diagram. In fact, only HCO^+ emission from the east side is found, suggesting that at these latitudes the lobe appears as a half-shell. In Fig. 3 (bottom-left panel) the p-v cut along the line joining the two central maxima of the HCO^+ emission (Fig. 2, direction "d") is plotted. This cut reveals a large velocity dispersion (~ 80 km s^{-1}) in the relatively compact region from which the maximum HCO^+ arises.

3.1.2. Excitation and abundance variations of HCO^+

Probably the most remarkable aspect of the HCO^+ emission is the presence of an intensity dip at low velocities (between 10–55 km s^{-1}) near the nebula center, where the rest of the observed molecular species reach their maximum intensity (for SO data see Figs. 5 and 6, and for CO see paper III). In fact, the most intense emission of this molecule arises from regions moving at high velocities with respect to the central star (Fig. 3). In order to state the origin of the HCO^+ intensity contrast between the slow, central component and the faster lobes, we will discuss the different factors that could affect the line intensity.

The central intensity dip of the HCO^+ line could be due to the presence of self absorption in the line. The importance of opacity effects has been evaluated through the $H^{12}CO^+/H^{13}CO^+$ ($J = 1$–0) intensity ratio, that in the nebula center is found to be $\gtrsim 8$ (see HCO^+ data in Sánchez Contreras et al., 1997, and in Fig. 4). This value agrees with the $^{12}C/^{13}C$ isotopic ratio estimated from CO data in regions in which the emission is known to be optically thin (Sánchez Contreras et al., 1997), and from the $H^{12}CN/H^{13}CN$ ($J = 1$–0) intensity ratio (see Sect. 3.4). We thus conclude that the HCO^+ lines are optically thin or only moderately opaque.

The regions with higher HCO^+ intensity could also correspond to regions of enhanced density. To check this possibility we have compared our HCO^+ observations with those of another high-density tracer, CS (see the CS and HCO^+ spectra within $\sim 27''$ – the beam FWHM – around the nebula center in Sánchez Contreras et al. 1997). The remarkable differences between the spectra of both species (note the maximum CS intensity around the systemic velocity) lead us to rule out a density effect as responsible for the strong HCO^+ emission enhancement in the lobes of OH 231.8+4.2. On the other hand, we have also studied the excitation conditions in OH 231.8+4.2 from the HCO^+ ($J = 1$–0)/($J = 3$–2) line intensity ratio assum-

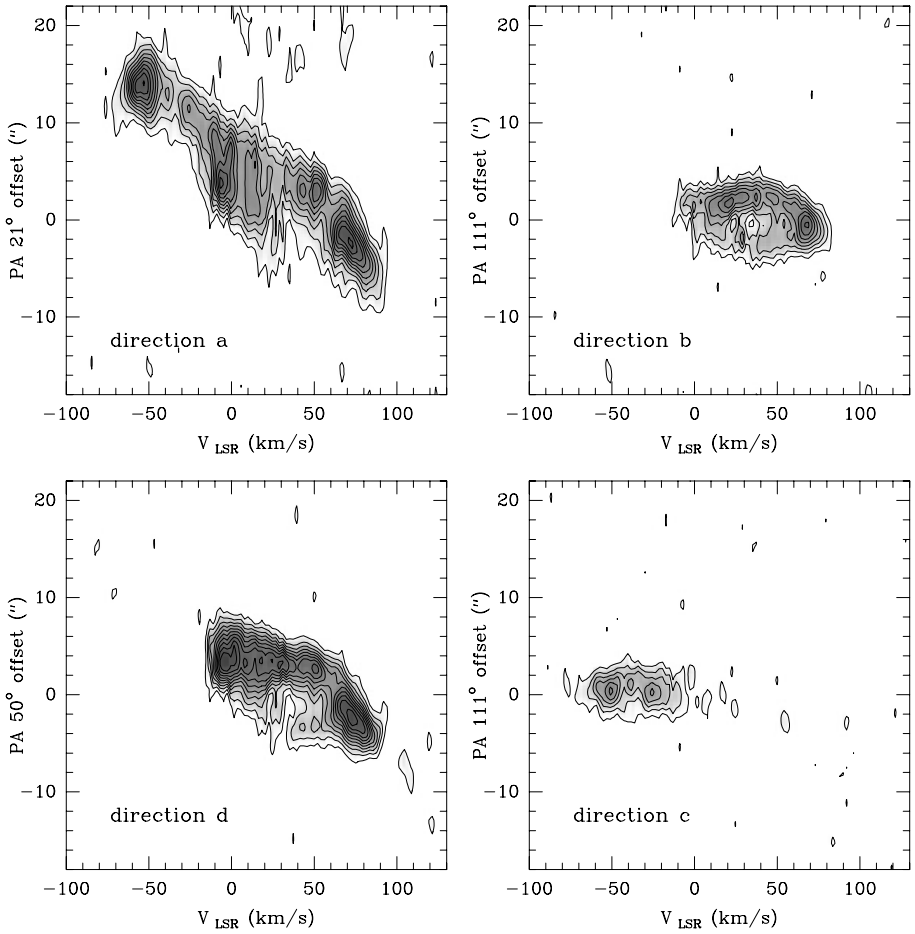

Fig. 3. HCO^+ position-velocity diagrams along the directions "a", "b", "c", and "d" indicated in Fig. 2. Levels are 10 to 100 by 10 mJy/beam.

ing that both transitions are optically thin. The brightness ratio of these lines is found to vary between ~ 2 (for velocities between –10:+50 km s^{-1}) and 0.8 (for velocities between 50–90 km s^{-1}), corresponding to (representative) excitation temperatures ($T_{\rm ex}$) of ~ 8 K and ~ 12 K, respectively. Note that the strong dependence of the previous ratio on $T_{\rm ex}$ (e.g. for $T_{\rm ex} = 6$ K the (1–0)/(3–2) ratio is ~ 5.7, ten times higher than for $T_{\rm ex} = 15$ K) limits the possible values of $T_{\rm ex}$ to a relatively small range. Excitation variations within this range cannot explain the strong intensity differences observed between the central, slow clumps and the outer, faster ones.

On the other hand, we note that the values of $T_{\rm ex}$ obtained for the HCO^+ lines are very similar to the kinetic temperature in the nebula estimated from the CO data (Sánchez Contreras et al., 1997). This could suggest that HCO^+, like CO, is thermalized and, therefore, that the gas density is, at least, $\sim 10^6$ cm^{-3} (the HCO^+ critical density).

In view of the previous discussion, we conclude that the observed intensity variations of HCO^+ are dominated by the real abundance variations of this molecule along the nebula: for some reason, this molecule is efficiently formed in the outer, accelerated clumps of OH 231.8+4.2. (For an estimate of the HCO^+ abundance in different clumps see Sánchez Contreras et al. 1997; note that the $T_{\rm ex}$ there assumed, 10 K, is very similar to the values here obtained.)

In our opinion, the efficient formation of HCO^+ in the lobes of OH 231.8+4.2 is very probably induced by shocks. The passage of shock fronts through the nebula (of which observational evidence exists, see Sect. 1) can modify the abundances dissociating stable molecules, followed by recombination favoring the formation of certain species like HCO^+, that is very rare in equilibrium chemistry (e.g. Neufeld and Dalgarno, 1989; see also discussion by Morris et al., 1987). A shock-induced chemistry would then explain the increase of the HCO^+ abundance in the post-shocked gas and, consequently, the particularly intense emission from this molecule in OH 231.8+4.2. We note that most of AGB envelopes (which usually do not show shock signs) show very weak or null HCO^+ emission (Cox et al., 1992, and references therein). This fact suggests that the high abundance of HCO^+ in OH 231.8+4.2 cannot be attributed to ionization by galactic UV photons since this source is not immersed in a particularly intense UV radiation field.

Ionization by stellar UV photons should also be ruled out as responsible for the HCO^+ abundance enhancement in the outer, fast flowing regions in OH 231.8+4.2. In fact, in the case of stellar photoionization the most intense emission should be observed in the inner regions of the molecular shell (see the case of CRL 618, Cox et al., 1992). On the other hand, the UV radiation by the central star of OH 231.8+4.2 is known to be very weak (Cohen, 1981; Cohen et al., 1985; Taylor & Morris, 1993). Re-

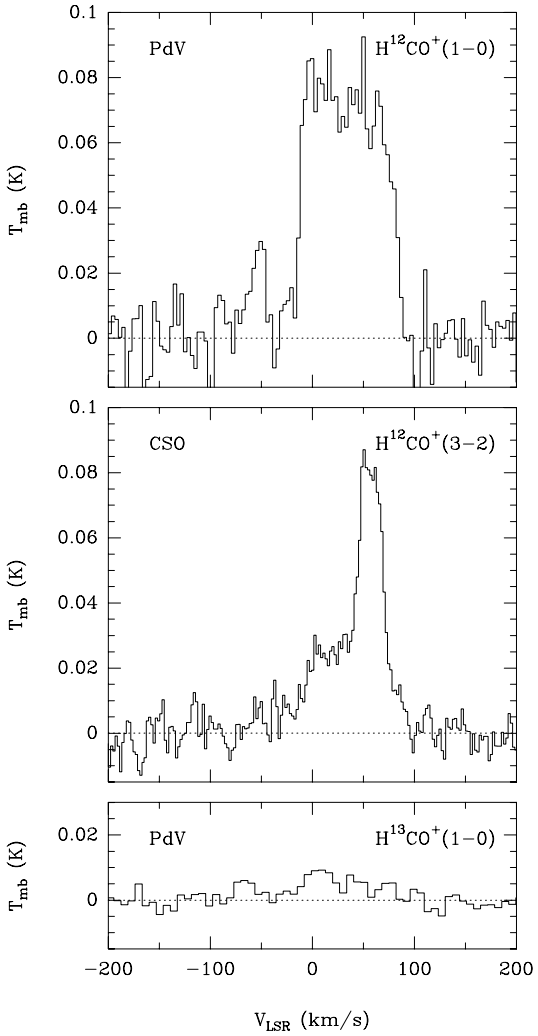

Fig. 4. $H^{12}CO^+$(J=1–0), $H^{12}CO^+$(J=3–2), and $H^{13}CO^+$(J=1–0) spectra at the nebula center.

actions involving high-energy particles have also been considered, since they are an efficient mechanism for producing HCO^+ in dense molecular clouds (Glassgold, 1996). Nevertheless, these processes, due to the large penetrating power of cosmic rays, would lead to an HCO^+ distribution similar to that of the other molecules, i.e. with the most intense emission arising from the most dense regions (the central clump in this case). Moreover, high energy particles, like galactic UV photons, should act in a similar way in AGB envelopes, that, as we have mentioned, show very weak or null HCO^+ emission.

3.2. SO

The distribution of the SO emission is found to be similar to that of CO (Sánchez Contreras et al., 1997; paper III), although significantly more compact (see Fig. 5). The SO emission occupies a narrow region ($\sim 10^{17}$ cm broad) that extends about $3.5\,10^{17}$ along the symmetry axis of the nebula. The total line width is about 100 km s^{-1}, indicating that SO is present in the accelerated lobes of OH 231.8+4.2. The peak of the SO emission (in contrast to HCO^+ and similarly to CO) arises from the central, slowly expanding component. From the SO p-v diagram along the nebula axis (Fig. 6) we can see that the SO emission follows the general velocity gradient along the symmetry axis of the nebula (the emission from the north/south lobe being blue/red-shifted). In addition, the SO emission reveals the presence of an expanding disk (or ring) that surrounds the central star. The presence of this inner, expanding disk is indicated by the inversion of the slope of the velocity gradient at the nebula center. In fact, in the PA 21° p-v diagram, we can see that in the densest, central $\sim 2''$ of the nebula, the velocity gradient has opposite sign (the north/south emission is red/blue-shifted) to that observed in the outer (weaker) regions of the nebula. Equatorial, expanding disks have been also detected in the inner molecular envelopes of other PPNe, leading to similar spectral features in p-v diagrams (see e.g. the case of M 1–92, Bujarrabal et al., 1998). The characteristic radius and the expansion velocity of the equatorial disk (or ring) of OH 231.8+4.2 deduced from our maps are $\sim 2\,10^{16}$ cm and $\sim$6–7 km s^{-1}, respectively. These values yield a kinematical age for the disk of about 1000 yr, very similar to that found for the bipolar molecular outflow (Sánchez Contreras et al., 1997). Nevertheless, the low velocity of the disk seems to indicate that this structure is a remnant of the old AGB envelope that has not been affected by the two-wind interaction that presumably accelerated the gas in the lobes of OH 231.8+4.2. No sign of rotation has been found in the disk (the rotational velocity should be less than 2 km s^{-1}; see the p-v diagram in the direction perpendicular to the nebula axis, Fig. 6), but the spatial resolution of these observations does not allow us to rule out some rotation in the innermost regions of OH 231.8+4.2 (see below). We have estimated the SO abundance (relative to H_2) in the equatorial disk and in the outflow (procedure and assumptions described in Sánchez Contreras et al. 1997) and have not found significant differences between the two components, for which we obtain a value of $\sim 10^{-6}$.

3.3. SiO maser

In Fig. 7 we show the SiO ($v = 1$, $J = 2$–1) maser spectra obtained in six different epochs. Three main spectral components can be distinguished at (LSR) velocities $\sim$26, $\sim$33, and $\sim$40 km s^{-1}. Since SiO masers usually arise from regions very close to the star, the centroid of the line is considered to be a reliable indicator of the stellar (or systemic) velocity ($V_{\rm sys}$), see Jewell et al. (1991). In the case of OH 231.8+4.2 we get $V_{\rm sys} \sim 33$ km s^{-1}, that approximately coincides with the peak of the CO emission (Sánchez Contreras et al., 1997) and the centroid of the SO line emission. Each of the three SiO features is formed of several subcomponents, indicating the complex and, probably, clumpy distribution of the gas in the vicinity of the central star. We are not able to spatially separate the regions from which the three (blue, systemic and red) components arise, and only an upper limit for the size of the emitting region of about ($0\farcs1$) $2\,10^{15}$ cm can be given. This value has been estimated from the direct analysis of the visibility phases for each spectral feature.

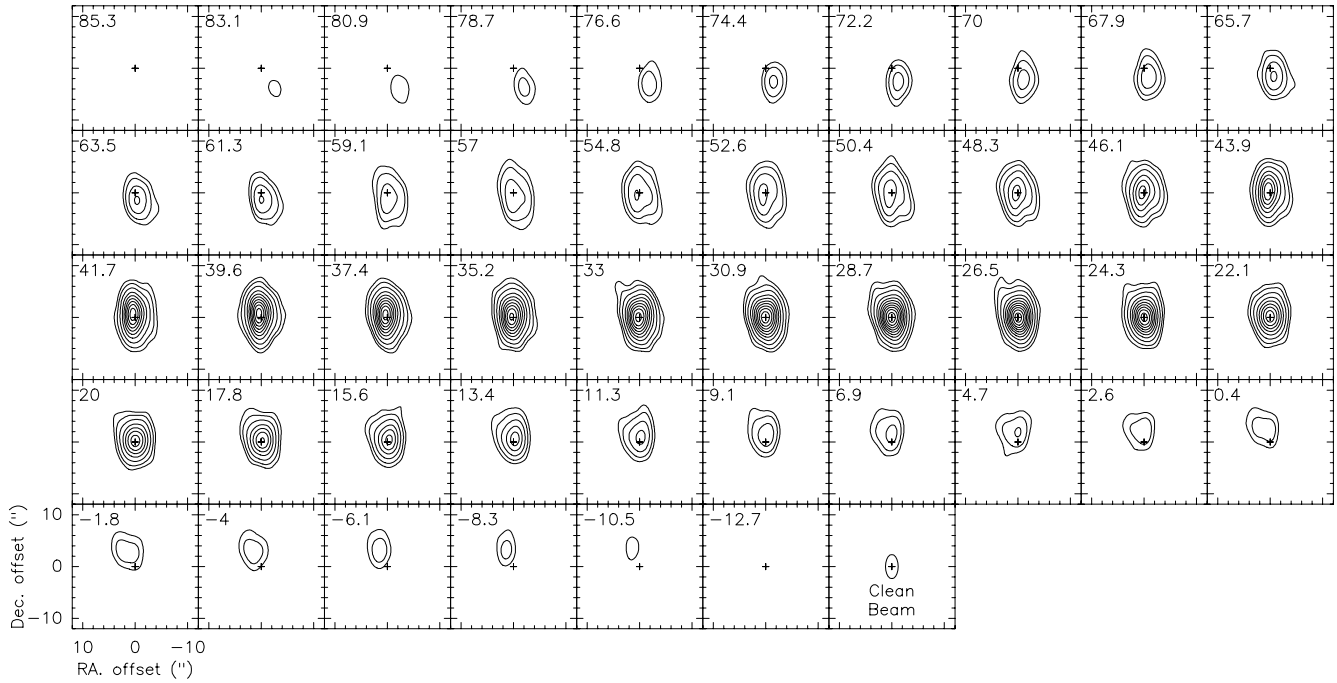

Fig. 5. SO maps at different LSR velocities (top-right corners). Levels are 20, 40, and 80 to 560 by 60 mJy/beam. The clean beam has a FWHM $4\farcs2\times2\farcs2$ and is oriented at PA = 0°. The conversion factor from flux units to brightness temperature is 14.6 K per Jy beam^{-1}. The rms of these maps is $\sim$ 4 mJy/beam.

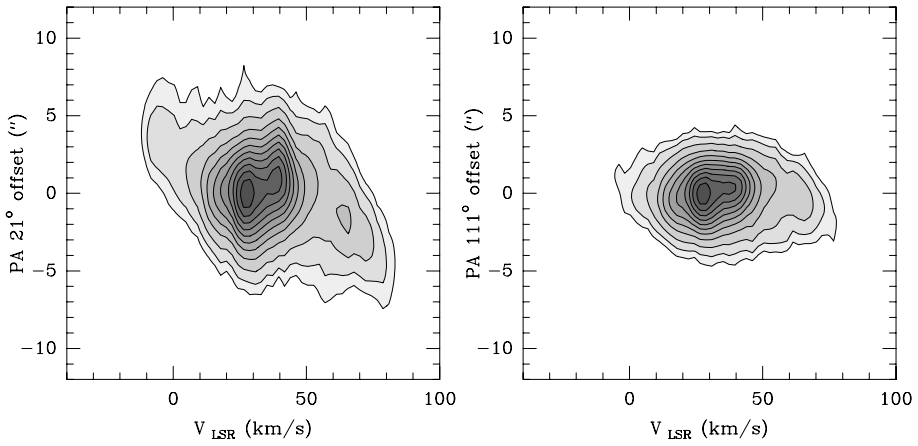

Fig. 6. SO position-velocity diagrams along the nebula axis (PA 21°) and the equator (PA 111°). Levels are the same that in Fig. 5. Note that the spatial and velocity box limits differ from those of the HCO^+ p-v diagrams.

The blue and red spectral components of the SiO maser line roughly coincide with the two intensity peaks of the H_2O maser at 22 GHz (Bowers & Morris, 1984). The spectral distribution of the OH maser (1667 MHz) is relatively flat in the LSR velocity range [–20:+80] km s^{-1} and possesses a narrow spike at +19 km s^{-1} (Bowers & Morris, 1984). The difference between the OH and SiO maser profiles is not surprising, since in OH 231.8+4.2 the OH maser emission occupies an extended region of $\sim 10''$ (Morris et al., 1982).

We would like to note that the blue and red spectral components of the maser roughly coincide with the blue and red intensity peaks of the SO disk emission (see Fig. 6). This fact, could suggest that the maser emission originates in the innermost regions of the expanding disk seen in the SO maps. The relatively stable SiO line structure (note that the same three spectral features appear in all the epochs in spite of the relative intensity variations between them) is in agreement with that idea. In this scenario, the systemic spectral component could arise from tangential maser amplification, and the blue and red ones, from the front and back regions of the disk, respectively. Our data would, indeed, indicate a small (or null) velocity gradient between the inner and outer parts of the disk traced by the maser and the SO thermal emission respectively. If it is confirmed that the SiO masers are distributed in an expanding disk close to the star, then the models requiring inner accretion disks or orbiting structures in the stellar vicinity (due to some kind of companion) to explain the onset of bipolarity in PNe (Soker & Livio, 1994; Jura et al., 1995; Mastrodemos & Morris, 1998, and references therein) should be substantially revised. However, the similar velocities of the blue and red intensity peaks of the maser and

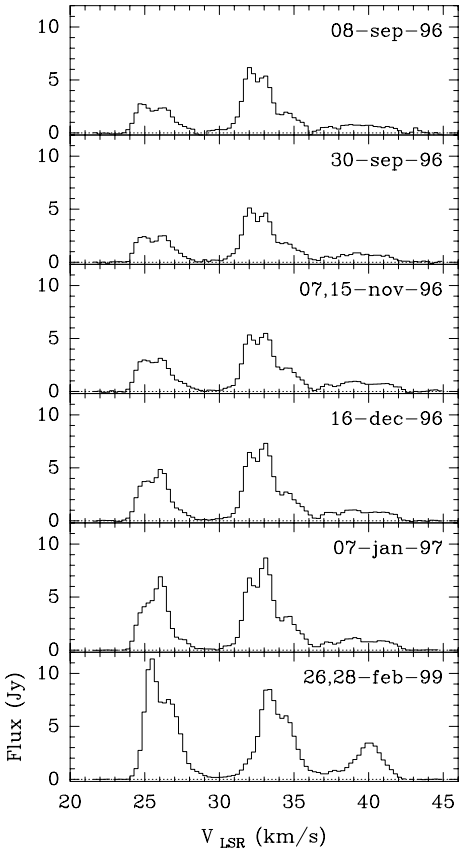

Fig. 7. SiO maser spectra for different epochs.

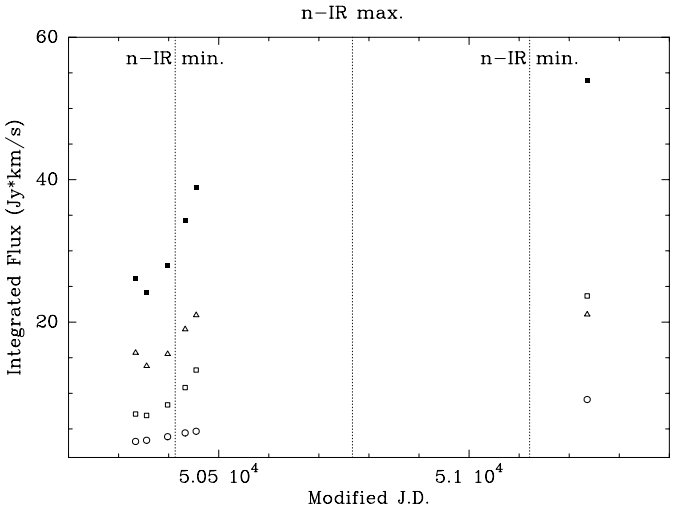

Fig. 8. SiO maser light curve for the three different spectral features of the line (blue: empty squares, systemic: triangles, and red: circles) and for the integrated intensity over the total line width (filled squares).

SO lines could be just an unlucky coincidence. In fact, for OH 231.8+4.2, rotation or infalling velocities are expected to be of the same order of magnitude ($\sim$ 5–8 km s^{-1}) at the distances where the masers originate (a few stellar radii). VLBI observations with about 0.″001 resolution are still needed to unveil the structure and kinematics of the inner regions of OH 231.8+4.2.

The relative intensity between the different spectral components and subcomponents as well as the total flux of the SiO line are found to strongly vary with time. In Fig. 8 we have plotted the maser intensity integrated over the total width of the line and over each of the three main (blue, systemic, and red) spectral features. In this figure, the epochs at which the maximum and minimum intensity of the near-infrared (n-IR) should have to occur (based on the n-IR light curve by Kastner et al., 1992) have been indicated by dotted-lines. We have found a relative minimum of the SiO flux $\sim$ 60 days before the n-IR minimum. Assuming that maser pumping is radiative, this phase lag would correspond to a distance of $\sim 10^{17}$ cm between the maser (very close to the star) and the nebular dust reflecting the n-IR starlight. This value is in agreement with the measured distance from the center to the region from which the maximum n-IR emission arises (Kastner et al., 1992; paper III).

3.4. H^{13}CN and NS

We have found the H^{13}CN (J = 1–0) emission to be distributed along the molecular outflow, sharing the general velocity gradient (see Fig. 9). The spectral and spatial distribution of this molecule is similar to that of SO, with the most intense emission arising from the slow, central component. Note that in this case we are not able to distinguish the inner expanding disk or ring seen from the SO emission. The H^{13}CN intensity peak does not lie at the systemic velocity (33 km s^{-1}) but at 28 km s^{-1}, that approximately corresponds to the blue peak of the SO disk emission.

From the H^{12}CN/H^{13}CN (J = 1–0) intensity ratio (H^{12}CN low-resolution maps were obtained with the 30 m IRAM radiotelescope, Sánchez Contreras et al. 1997) and assuming that both lines are optically thin, we deduce an isotopic ^{12}C/^{13}C ratio of $\sim$ 5–10. This value is in agreement with that found from the ^{12}CO/^{13}CO (J = 1–0) intensity ratio of the line wings, which are optically thin (Sánchez Contreras et al., 1997). Such a value is lower than that predicted by standard evolutionary models ($\gtrsim$ 20), and is often observed in evolved stars (Charbonnel, 1995; Palla et al., 1998). The ^{13}C abundance enhancement has been attributed to a nonstandard mixing mechanism that operates during the red giant phase.

We also report the first detection of nitrogen sulfide (transition $^2\Pi_{1/2}$, J = 5/2–3/2, parity-e) in circumstellar envelopes (Fig. 10). The NS emission is distributed in a compact central region and in the outflow (note the relatively large width of the line). The total flux of the line (integrated over all the hyperfine components) is relatively high, $\sim$ 15 Jy km s^{-1}. The intensity ratio between the 3 highest and the 2 weakest hyperfine components is in agreement with the theoretical value (considering the different strength of each hyperfine line component, McGonagle et al. 1994) suggesting that the line is optically thin. This fact allows us to estimate the NS abundance (relative to H_2) in the central clumps of OH 231.8+4.2. Assuming $T_{\rm ex}$ = 10 K and the mass of the central clumps (–30:+80 km s^{-1}) to be $\sim 0.5\,M_\odot$ (see Sánchez Contreras et al. 1997) an abundance of $\sim 2\,10^{-8}$ is found.

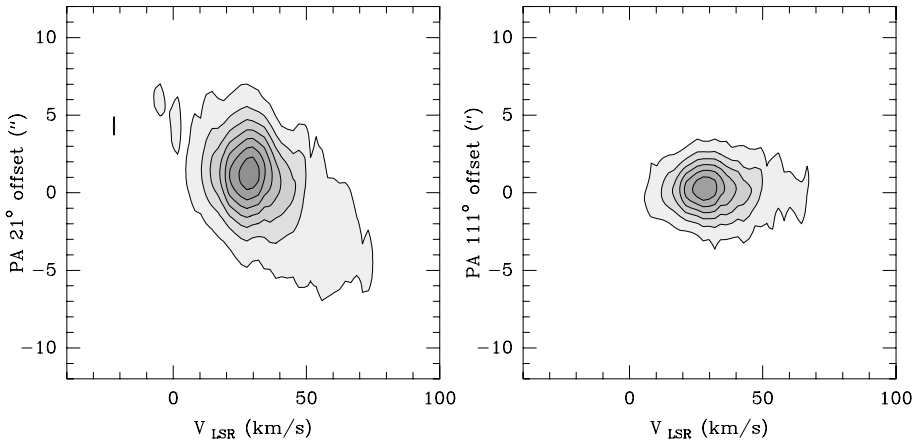

Fig. 9. $H^{13}CN$ position-velocity diagrams along the nebula axis (PA 21°) and the equator (PA 111°). The clean beam has a FWHM $4\farcs6\times2\farcs4$ and is oriented at PA=0°. Levels are 20 to 260 by 40 mJy/beam. The rms of these maps is $\sim$4 mJy/beam. The conversion factor from flux units to brightness temperature is 14.5 K per Jy beam^{-1}. Note that the effective spectral resolution is degraded by the hyperfine structure of the molecule.

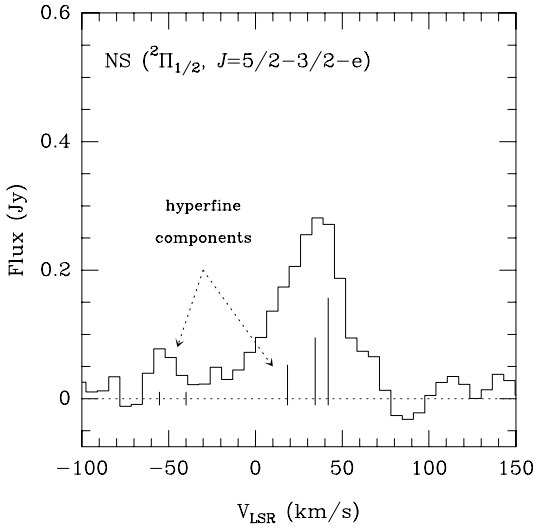

Fig. 10. NS spatially integrated spectrum. Note the hyperfine structure indicated by the ticks over the dotted line. The length of the ticks indicates the relative strength of the different components.

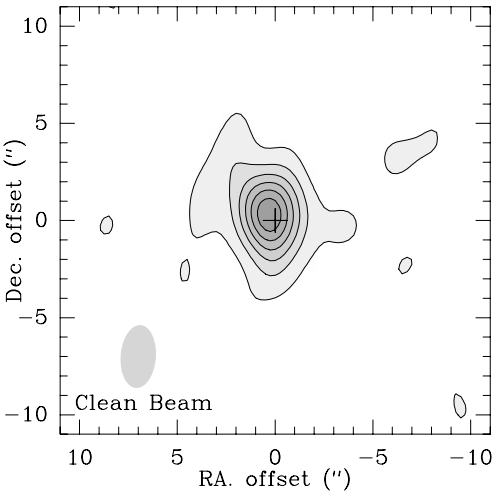

Fig. 11. Continuum emission at 3 mm. Levels are 1 to 11 by 2 mJy/beam. The FWHM of the clean beam is $3\farcs2\times1\farcs8$. The rms of this map is 0.5 mJy/beam.

The large variety and abundance of nitrogen- and sulfur-bearing molecules in OH 231.8+4.2 is a clear sign of an active chemistry that is probably induced by shocks. Shocks would initiate (endothermic) reactions that trigger the N and S chemistry (e.g. $N^+ + H_2 \rightarrow$..., and $S^+ + H_2 \rightarrow$...; Lada et al. 1978) and could also extract additional S from the surface of dust grains (Jackson & Nguyen-Q-Rieu, 1988).

3.5. Continuum at λ = 3 mm

The 3 mm ($\sim$87.8 GHz) continuum map of OH 231.8+4.2 is shown in Fig. 11. The continuum is found to slightly extend along the nebula axis. From our mapping we obtain that the 3 mm continuum can be separated in an extended ($\sim$18 mJy) and a point-like ($\sim$7 mJy) component. The continuum total flux obtained from these observations, is in agreement with that obtained from single-dish millimeter observations (see below), showing that flux losses by the interferometer are negligible. The extended component is roughly elongated along the symmetry axis of the nebula, with a total length of $\sim8''$. The previous separation in components has been established by fitting different structure models directly to the visibilities. The best fit was obtained when assuming a point+'elliptic gaussian' source. The structure and the fluxes obtained for the two components of the continuum at 3 mm are in agreement with the general properties of the continuum emission at millimeter wavelengths in this source (Sánchez Contreras et al., 1998). These authors attribute the extended mm-continuum emission to cold dust ($\sim$20 K) distributed along the lobes of the nebula. The point-like emission would be due to a compact region of warmer dust ($\sim$55 K) around the central star.

4. Conclusions

We have obtained high spatial resolution ($2''$–$4''$) maps of OH 231.8+4.2 in several molecular lines – HCO^+ (J=1–0), SO (J=2_2–1_1), $H^{13}CN$ (J=1–0), SiO (v=1, J=2–1) and NS ($^2\Pi_{1/2}$, J=5/2–3/2, parity-e) – and the continuum at 3 mm. The main conclusions reached in this work are:

– All the molecules are distributed in a narrow region along the symmetry axis, and flow outwards following a velocity gradient similar to that found in CO (Alcolea et al., in preparation).
– Except for HCO^+, the most intense emission from all the molecules arises from the nebula center, from a relatively compact, slowly expanding component that could be the non-accelerated remnant of the envelope ejected by the star during the AGB.
– In the nebula center, HCO^+ is distributed in an expanding, hollow cylinder. In the equatorial direction, the HCO^+ emission is slightly more extended than that of ^{12}CO and other molecules.
– The HCO^+ emission is found to be very clumpy and strongly enhanced in the shock-accelerated lobes. This intensity enhancement can only be explained by an increase of the HCO^+ abundance in these regions. In our opinion, the efficient formation of this radical in the outer, fast flowing clumps is probably induced by shocks.
– The SO maps have revealed the presence of an expanding, equatorial disk or ring around the central star. The characteristic radius and the expansion velocity of this structure are $\sim 2\,10^{16}$ cm and $\sim$ 6–7 km s^{-1}, respectively.
– The spectral distribution and the small extent of the SiO maser emission suggest that it arises from the innermost parts of the expanding disk. The intensity and profile of the different spectral features of the line have been found to strongly vary with time. The good agreement between the SiO and n-IR light curves suggests radiative maser pumping.
– We report the first detection of NS in circumstellar envelopes with a relative abundance of $2\,10^{-8}$.
– The large variety of S- and N-containing molecules indicates that an active chemistry, that (like in the case of HCO^+) could involve shock-induced reactions, takes place in OH 231.8+4.2.
– The 3 mm continuum emission seems to arise from cold ($\sim$ 20 K) dust distributed along the nebular lobes as well as from a warmer ($\sim$ 55 K) dust component arising from a compact region surrounding the central star.

Acknowledgements. We are grateful to A. Castro-Carrizo and J.R. Pardo for obtaining the HCO^+(3–2) spectrum. C. Sánchez Contreras acknowledges the support of the Universidad Complutense de Madrid through a predoctoral fellowship and a travel grant. This work was partially supported by the Spanish DGES, project numbers PB96-0104.

References

Alcolea J., Bujarrabal V., Sánchez Contreras C., 1996, A&A 312, 560
Bowers P.F., Morris M., 1984, ApJ 276, 646
Bujarrabal V., Alcolea J., Sahai R., Zamorano J., Zijlstra A.A., 1998, A&A 331, 316
Charbonnel C., 1995, ApJ 453, L41
Cohen M., 1981, PASP 93, 288
Cohen M., Dopita M.A., Schwartz R.D., Tielens A., 1985, ApJ 297, 702
Cox P., Omont A., Huggins P., Bachiller R., Forveille T., 1992, A&A 266, 420
Diamond P.J., Kemball A.J., Junor W., et al., 1994, ApJ 430, L61
Genzel R., Downes D., 1977, A&AS 30, 145
Glassgold A.E., 1996, ARA&A 34, 241
Guilloteau S., Delannoy J., Downes D., et al., 1992, A&A 262, 624
Jackson J.M., Nguyen-Q-Rieu, 1988, ApJ 335, L83
Jewell P.R., Snyder L.E., Walmsley C.M., Wilson T.L., Gensheimer P.D., 1991, A&A 242, 211
Jura M., Balm S.P., Kahane C., 1995, ApJ 453, 721
Kastner J.H., Weintraub D.A., Merrill K.M., Gatley I., 1998, AJ 116, 1412
Kastner J.H., Weintraub D.A., Zuckerman B., et al., 1992, ApJ 398, 552
Lada C.J., Oppenheimer M., Hartquist T.W., 1978, ApJ 226, L153
Mastrodemos N., Morris M., 1998, ApJ 497, 303
McGonagle D., Irvine W.M., Ohishi M., 1994, ApJ 422, 621
Morris M., Bowers P.F., Turner B.E., 1982, ApJ 259, 625
Morris M., Guilloteau S., Lucas R., Omont A., 1987, ApJ 321, 888
Neufeld D.A., Dalgarno A., 1989, ApJ 340, 869
Palla F., Galli D., Bachiller R., Pérez-Gutiérrez M., 1998, Space Sci. Rev. 84, 177
Reipurth B., 1987, Nat 325, 787
Sánchez Contreras C., Alcolea J., Bujarrabal V., Neri R., 1998, A&A 337, 233
Sánchez Contreras C., Bujarrabal V., Alcolea J., 1997, A&A 327, 689
Sánchez Contreras C., Bujarrabal V., Fernández-Figueroa M.J., Miranda L.F., 2000, A&A, in press
Shure M., Sellgren K., Jones T.J., Klebe D., 1995, AJ 109, 721
Soker N., Livio M., 1994, ApJ 421, 219
Taylor G.B., Morris M., 1993, ApJ 409, 720
Woodward C.E., Forrest W.J., Pipher J.L., Moneti A., Shure M.A., 1989, ApJ 337, 754